Imprint Efficiency Measurements in Laser-Driven Plastic Foils Using Beams with Different Angles of Incidence

Introduction

The goal of the direct-drive approach to inertial confinement fusion (ICF)[1,2] is to uniformly implode a spherical target with deuterium–tritium (DT) fuel using a large number of overlapped laser beams. A combination of high temperature and high areal density (ρR) in the DT fuel at peak compression is necessary to ignite the target and achieve high gain.[1–3] The most-significant factor that limits the implosion performance is the unstable growth of target perturbations. As a result of this growth, the fuel temperature and compression may be reduced, leading to a reduction in the thermonuclear yield. The target perturbations in direct-drive ICF include existing imperfections of the inner and outer target surfaces and are dominated by modulations seeded (or imprinted) by the spatial laser nonuniformities;[4–29] therefore, understanding and controlling laser imprinting are crucial to the success of direct-drive ICF.

Spatial modulations in laser intensity are imprinted into the target in the first few hundred picoseconds of the drive. As the laser light is applied to the target, the pressure created by the target ablation launches a shock wave that compresses the target.[30,31] Any nonuniformities in the laser drive modulate the ablation pressure. The modulations in surface acceleration provide the seeds for hydrodynamic instabilities. Later, as a large volume of plasma develops, the laser modulations decouple from the target surface, smoothing the ablation pressure. The imprinted front-surface (or ablation-surface) perturbations continue to evolve as the shock-driven Richtmyer–Meshkov (RM) instability causes the modulations to grow; the ablation stabilizes this growth.[18,32] As a result, the ablation-surface nonuniformities oscillate during the shock propagation to the rear surface of the target. The amplitude and frequency of these oscillations are defined by the modulation wavelength, the sound speed, the ablation, and the expanding (or "blowoff") plasma velocities.[32] Because the shock is launched by a modulated laser drive, the shock front is also distorted. The amplitude of this distortion oscillates as it propagates through the target with a frequency determined by the modulation wavelength and the drive intensity.[30,31] When the shock front reaches the rear surface of the target, it sends the rarefaction wave back to the ablation surface; shortly thereafter, the target starts to accelerate. During the acceleration phase, the ablation-surface modulations grow exponentially due to Rayleigh–Taylor (RT) instability.[2,3]

A number of techniques have been developed to reduce laser imprinting in direct-drive ICF facilities. A combination of distributed phase plates (DPP's),[33] polarization smoothing (PS),[34] and smoothing by spectral dispersion (SSD)[35] is employed on the OMEGA laser.[36] Induced spatial incoherence (ISI)[37] is used on the NIKE laser system. Partially coherent light (PCL)[38] in combination with random-phase plates is used on the GEKKO-XII laser facility. Targets with foam-buffered layers, high-Z overcoat, and a combination of the two have been demonstrated to reduce imprinting.[5–7,11,16,20,23–25,27–29]

The first measurements[5] of laser-imprinted modulations were performed using a side-on geometry, where the diagnostic x rays penetrate a planar target in the direction perpendicular to its motion. Almost all subsequent imprinting studies were performed using a face-on geometry where the diagnostic x rays penetrate the target in the direction along its motion, allowing more-quantitative measurements of target perturbations. Face-on radiography is sensitive to variations in the target density thickness, or areal density (ρR), which includes not only the ablation-front modulations (existing or laser imprinted), $\delta\left[\rho R_{\mathrm{abl}}(t)\right]$ at time t, but also any shock-front modulation in the bulk of the target, $\delta\left[\rho R_{\mathrm{sh}}(t)\right]$:

$$\delta\left[\rho R(t)\right] = \delta\left[\rho R_{\mathrm{abl}}(t)\right] + \delta\left[\rho R_{\mathrm{sh}}(t)\right]. \qquad (1)$$

Early imprint experiments[8–10,12,14,15,17–19] were performed at or before shock breakout on the rear surface of the target (before the onset of the RT growth), when the ablation- and shock-front modulations are of the same order of magnitude, $\delta\left[\rho R_{\mathrm{abl}}(t)\right] \cong \delta\left[\rho R_{\mathrm{sh}}(t)\right]$. Intended to be measurements of the ablation-surface imprinted perturbations (initial seed for the RT instability), the resulting areal-density modulations also included the shock-front perturbations.[30,31] Later experiments

observed shock-front and ablation-surface evolutions during shock transit before the beginning of the RT growth.[30,31,39–41]

To quantify imprinted modulation levels, imprint efficiency measurements[10,14,26] have used the acceleration-phase RT growth to magnify the ablation-front modulations in order to separate them from the shock-front modulations. Figure 98.26 (from Ref. 34) schematically presents the idea behind these experiments using simulations by the 2-D code *ORCHID*.[42] The solid curve shows the evolution of the areal-density modulation of an initially smooth target driven by a laser having a single-mode intensity modulation at 60-μm spatial wavelength, while the dotted curve shows the evolution of the single-mode, 60-μm-wavelength, preimposed perturbation driven by a spatially perfect laser. The solid curve starts at zero and rises as imprinting begins, while the dotted curve starts at its preimposed level. The RT growth (starting at ~400 ps) amplifies the imprinted and imposed ablation-front perturbations in the same manner and, when ablation-front modulations become higher than shock-front modulations, $\delta\left[\rho R_{\mathrm{abl}}(t)\right] > \delta\left[\rho R_{\mathrm{sh}}(t)\right]$, the areal-density evolutions become similar (dotted and solid curves are parallel after 0.5 ns). The equivalent surface amplitude of imprinting at a particular mode number k is defined by extrapolating (dashed curve) the temporal evolution of the imprinted modulation (solid curve) back to $t = 0$ using the behavior of the preimposed mode (dotted curve):

$$\eta_{\mathrm{imp}}(k,t=0) = \eta_{\mathrm{pre}}(k,t=0) \times \left\{\delta\left[\rho R_{\mathrm{imp}}(k,t)\right] \Big/ \delta\left[\rho R_{\mathrm{pre}}(k,t)\right]\right\}, \qquad (2)$$

where $\eta_{\mathrm{pre}}(k,t=0)$ is the initial amplitude of the preimposed modulation and $\delta\left[\rho R_{\mathrm{imp}}(k,t)\right]$ and $\delta\left[\rho R_{\mathrm{pre}}(k,t)\right]$ are the measured areal-density modulations of imprinted and imposed perturbations during linear RT growth, respectively. This technique is valid when (1) the amplitudes of imprinted and preimposed modulations are in the linear regime of the RT growth, and (2) the measurements are taken when the ablation-front modulations are large enough to dominate the measurements. The imprint efficiency $E(k)$ was defined[10,14] as the initial amplitude of equivalent surface modulation $\eta_{\mathrm{imp}}(k,t=0)$, normalized to the relative laser modulation $\delta I(k)/I$, that produced it:

$$E(k) = \eta_{\mathrm{imp}}(k,t=0) \Big/ \left[\delta I(k)/I\right]. \qquad (3)$$

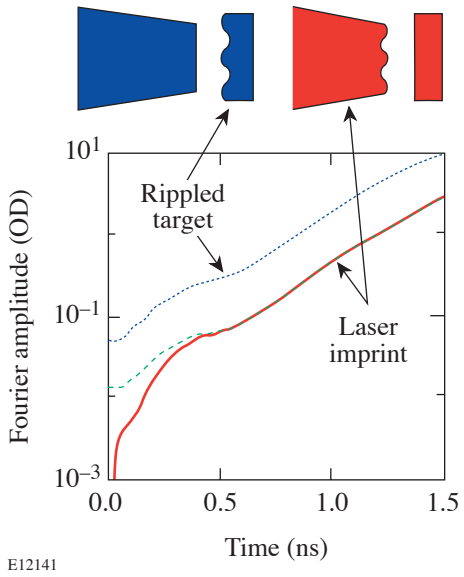

Figure 98.26
Definition of the equivalent surface amplitude using an *ORCHID* simulation of a single-mode, 60-μm-wavelength, imprinted modulation (solid curve) calibrated to a preimposed (dotted curve) modulation (from Ref. 34). The equivalent surface amplitude of imprinting at a particular mode number k is defined by extrapolating (dashed curve) the temporal evolution of the imprinted modulation (solid curve) back to $t = 0$, using the behavior of the preimposed mode (dotted curve) and Eq. (2).

In direct-drive implosions, a spherical shell is illuminated by a large number of overlapping laser beams. Each beam diameter is roughly equal to that of the target; therefore, different parts of the beam irradiate the target at different angles of incidence: the central part of the beam is nearly normally incident to the target, while the outer parts of the beam irradiate the target at oblique angles. As a result it is important to investigate the effect of the beam angle of incidence on imprint efficiency. Recently, the imprint efficiency measurements for three different angles of incidence were performed for the first time in targets and laser intensities relevant to the spherical implosion program on OMEGA.[43] This article presents details of the techniques and analysis of the imprint efficiency measurements and is considered complimentary to Ref. 43.

Experimental Configuration

Figure 98.27(a) shows schematically the experimental configuration, previously used in a number of experiments.[20–22,26,34] The 20-μm-thick plastic targets were irradiated by 351-nm laser light at ~2 × 10^{14} W/cm^2 using seven overlapped beams with a 3-ns square pulse shape on the

OMEGA laser system.[36] The imprint efficiencies at 60-μm spatial wavelength were with and without 0.2-THz SSD.[35] Targets with preimposed, single-mode, two-dimensional, 60-μm sinusoidal perturbations were used to determine the imprint efficiency: one target with 0.125-μm initial amplitude and the other with 0.05-μm initial amplitude. The temporal growth of target perturbations was measured using x-ray, face-on radiography. The targets were backlit with x rays produced by a uranium backlighter located 9 mm away from the driven foil and irradiated at ~1×10^{14} W/cm^2 using 12 additional beams. X rays transmitted through the target and a 3-μm-thick aluminum debris shield (located between the backlighter and the driven foil) were imaged by the 8-μm pinhole array on a framing camera filtered with 6 μm of aluminum.[20–22] This yielded the highest sensitivity for the average photon energy of ~1.3 keV. The distance between the target and the pinhole array was 2.5 cm, and the magnification was 14.4. The framing camera recorded eight images in each shot with a temporal resolution of ~80 ps and a spatial resolution in a target plane of ~10 μm.[44] The framing camera images were captured on Kodak T-Max 3200 film, which was digitized with a 20-μm-sq scanning aperture. The measured target optical depth (which is proportional to the target areal density) is the natural logarithm of the intensity-converted images of a target.

Figure 98.27(b) shows the laser-beam configuration. Six beams (numbers 34, 36, 38, 41, 43, and 49) were incident at 23° to a target normal, while one beam (number 48) was incident at 48° to a target normal. The 23° beams had DPP's[33] and PS.[34] An equivalent-target-plane image of one such beam is shown in Fig. 98.28(a). These beams had a broadband spectrum of modulations with the smallest features having spatial wavelengths of ~2.5 μm. Beam 48 [shown in Fig. 98.28(b)], incident at a more-oblique 48° angle, had 2-D, 60-μm-wavelength intensity modulations (together with several higher harmonics) to distinguish it from the 23° beams. The beam modulations were oriented along the direction of its propagation, so the imprinted target modulations had the same wavelengths as the laser modulations. The 2-D laser modulations were used to

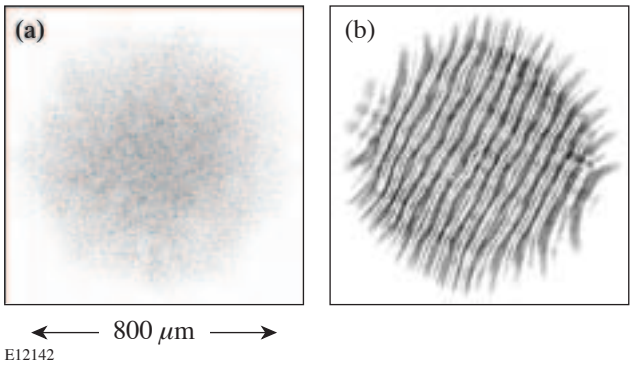

Figure 98.28
Beam images of the (a) 23° beam having 3-D broadband perturbations and (b) 48° beam having 2-D, 60-μm-wavelength perturbation.

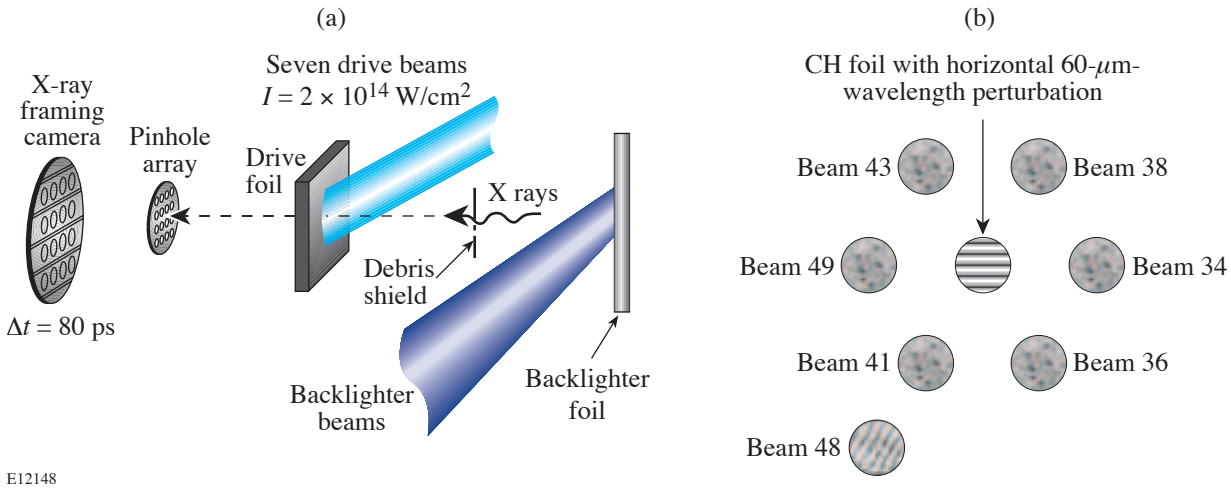

Figure 98.27
(a) Experimental configuration (from Ref. 22); (b) beam and target configuration. Diagonal 2-D perturbations at 60-μm wavelength come from beam 48 incident at 48° to a target normal, while 3-D broadband perturbations come primarily from beams 34, 36, 38, 41, 43, and 49 incident at 23° to the target normal. The target has a horizontal, preimposed, single-mode, 60-μm-wavelength perturbation used for calibration.

separate perturbations caused by the 48° beam from the 3-D broadband modulations caused by the 23° beams in the radiogram of the driven target. Figure 98.29(a) shows the profile of the relative intensity incident on the target (averaged in the direction along the 2-D perturbations), calculated using measured beam intensities [Figs. 98.28(a) and 98.28(b)] and taking into account experimentally measured beam energies, effects of beam overlap, and obliquity angles. Figure 98.29(b) presents the Fourier amplitude of this lineout showing the laser perturbations at 60-μm wavelength (together with the higher harmonics) clearly distinguishable from the other broadband laser modulations. The laser modulations were analyzed in nine different square areas (with a box size of $L = 300$ μm, the same size as in the target x-ray radiographs shown later) of ~800-μm laser spots, and it was found that the modulations were reasonably constant across the laser-spot size. The amplitudes of relative laser modulations at a spatial frequency of 17 mm^{-1} (corresponding to a spatial wavelength of 60 μm) were 6.3±0.4% for the two-dimensional modulation (from the 48° beam) and 0.54±0.09% for the broadband modulations (from the 23° beams), as calculated in the nine different areas.

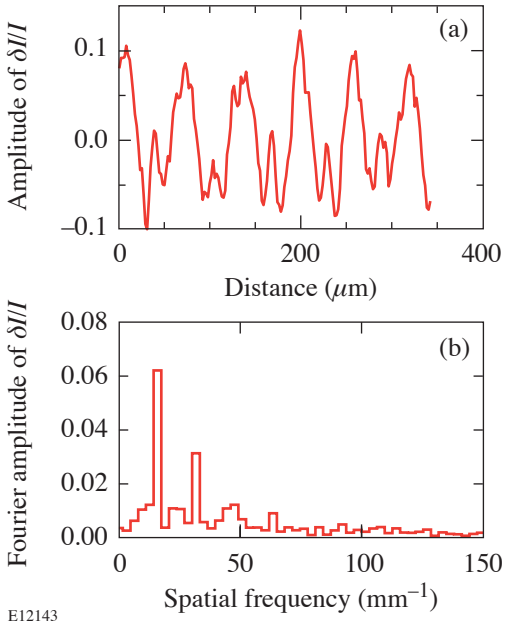

Figure 98.29
(a) Profile of the relative intensity incident on the target averaged in the direction along the 2-D laser perturbations. (b) Fourier amplitude of this profile showing the laser perturbations at a spatial frequency of 17 mm^{-1} (corresponding to the 60-μm wavelength) together with the higher harmonics clearly distinguishable from the other broadband laser modulations.

Experimental Results

Figure 98.30(a) presents one of the eight images of target optical-depth modulations taken at ~1.9 ns after the beginning of the laser drive for the shot without SSD. The corresponding Fourier-space image of the target optical-depth modulations is shown in Fig. 98.30(b). Two-dimensional perturbations, imprinted from the 48° beam, are diagonal across the real-space image; they have distinctive first- and second-harmonic peaks in the Fourier-space image. The preimposed, 60-μm-wavelength perturbation is horizontal in the real-space image; therefore it has two vertical peaks in the Fourier-space image. The 3-D features in the real-space image are imprinted from the broadband perturbations of 23° beams; these perturbations are located in the broad area of the Fourier-space image. The profiles of the 2-D imprinted and preimposed modulations are presented in the Fig. 98.31. Figure 98.31(a) shows the optical-depth profile of the 2-D imprinted modulation averaged along the modulations, while Fig. 98.31(b) shows the profile of the 2-D preimposed modulation, averaged along the horizontal direction. The higher optical depth corresponds to thinner areas of the targets, or bubbles, while the lower optical depth corresponds to thicker target areas, or spikes. The profile of the imprinted optical-depth modulation resembles the profiles of the laser modulation [compare Figs. 98.29(a) and 98.31(a)].

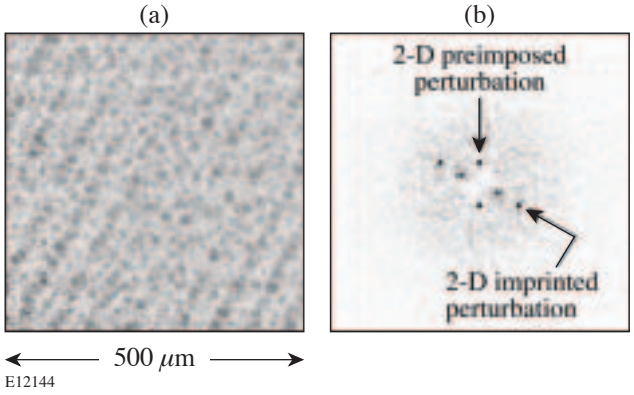

Figure 98.30
(a) Image of the target optical-depth modulations taken at ~1.9 ns after the beginning of the laser drive for the shot without SSD. (b) Fourier-space image of the target optical-depth modulations showing peaks for a diagonal 2-D, 60-μm wavelength and its second-harmonic imprinted modulations, and 2-D, 60-μm-wavelength, preimposed modulations in the vertical direction.

Figure 98.32 summarizes the results of the measured growth for all 60-μm-wavelength perturbations with imprinted modulations shown in Fig. 98.32(a) and preimposed modulations in Fig. 98.32(b) for two shots with and without SSD. Two-dimensional imprinted modulations from the 48° beam are

shown by the upper data (diamonds) in Fig. 98.32(a), and 3-D broadband modulations from the 23° beams are shown by the lower data (squares). The amplitudes of imprinted modulations are separated by about 0.5 ns in shots with and without SSD [Fig. 98.32(a)]. This is because the SSD reduces the initial amplitudes of imprinted modulations by a factor of ~2.5, and it takes longer for the RT growth to bring them to the same levels as for the shot without SSD. The initial amplitudes of preimposed modulations were 0.125 μm and 0.05 μm for the shots without and with SSD, respectively.

To satisfy the conditions for imprint efficiency measurements described in the **Introduction**, the growth measurements of 60-μm-wavelength perturbations were performed in the linear regime of RT instability. To confirm that the measured modulations were below the RT saturation levels, ablation-front amplitudes $\eta(k,t)$ were estimated from the measured optical-depth modulations OD(k,t), the measured undriven target attenuation length λ_{eff} = 10 μm, and the calculated (1-D hydrocode *LILAC*)[45] target compression $C_p \sim 3$, $\eta(k,t) = \text{OD}(k,t) \times \lambda_{\text{eff}} / C_p$. The amplitudes of 2-D, single-mode perturbations were calculated to be below 1 μm at all times for both shots (the 2-D saturation amplitude for the λ = 60-μm wavelength is $S_{2\text{-D}}$ = 6 μm), and the amplitudes of 3-D, broadband perturbations were calculated to be below 0.1 μm in the square analysis area with a size of L = 300 μm [the 3-D saturation amplitude[46,21] for the λ = 60-μm wavelength is $S_{3\text{-D}} = \lambda^2/(2\pi^2 L) \cong 0.3\,\mu\text{m}$]. All measurements were performed 1.0 ns after the beginning of the drive, when the growth of imprinted and preimposed modulations was similar. All three types of target modulations (2-D imprinted, 2-D preimposed, and 3-D imprinted) at 60-μm wavelength grow with similar growth rates for each shot, as shown in Fig. 98.32. The solid lines in Fig. 98.32 show exponential fits to the experimental data. The inferred growth rates were 1.7±0.2 ns^{-1}, 1.5±0.2 ns^{-1}, and 1.6±0.2 ns^{-1} for the 2-D imprinted, 2-D preimposed, and 3-D imprinted modulations, respectively, for the shot without SSD. The corresponding growth rates for the shot with SSD are 1.7±0.3 ns^{-1}, 2.0±0.3 ns^{-1}, and 2.1±0.3 ns^{-1}.

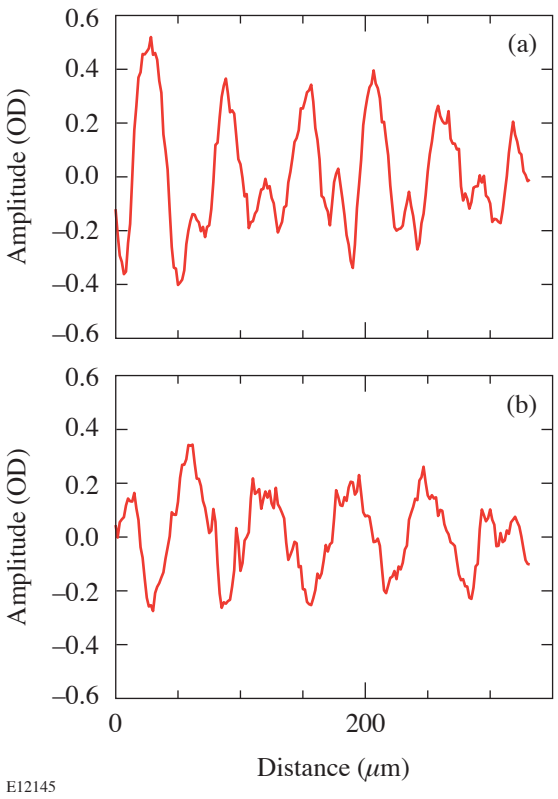

Figure 98.31
Optical-depth profiles of (a) the 2-D imprinted modulation and (b) the 2-D preimposed modulation taken at ~1.9 ns after the beginning of the laser drive.

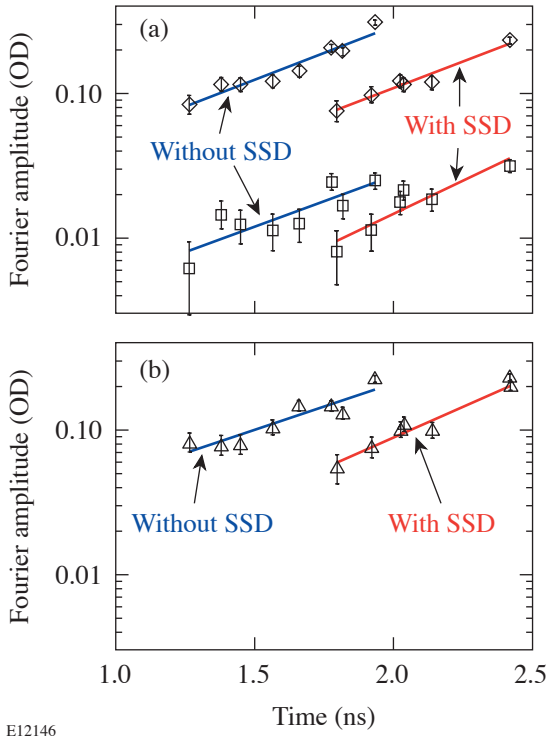

Figure 98.32
Fourier amplitudes of optical-depth modulations as a function of time for (a) 2-D imprinted modulations (diamonds, upper data), 3-D broadband modulations (squares, lower data), and (b) the 2-D preimposed modulations (triangles). Data with SSD comes later than the data without SSD.

The surface equivalent amplitude of an imprinted 2-D, 60-μm-wavelength perturbation from a 48° beam was $\eta_{\text{imp 2-D}}(t = 0) = 0.16\pm0.01$ μm, from Eq. (2). The initial modulation amplitude of 2-D preimposed modulation $\eta_{\text{pre 2-D}}(t = 0) = 0.125$ μm, and the ratios of measured optical-depth modulations at various times,

$$\delta\left[\rho R_{\text{imp 2-D}}(k,t)\right] \Big/ \delta\left[\rho R_{\text{pre 2-D}}(k,t)\right],$$

taken from Figs. 98.32(a) and 98.32(b). The surface equivalent amplitude of 3-D imprinted, 60-μm-wavelength perturbations from 23° beams was $\eta_{\text{imp 3-D}}(t = 0) = 0.016\pm0.001$ μm. The imprint efficiencies at 60-μm wavelength for 48° and 23° beams were $E_{48°} = 2.5\pm0.2$ μm and $E_{23°} = 3.0\pm0.3$ μm, respectively, as calculated using Eq. (3) and relative laser modulations $[\delta I(k)/I]_{48°} = 6.3\pm0.4\%$ for the 48° beam and $[\delta I(k)/I]_{23°} = 0.54\pm0.04\%$ for the 23° beams at a spatial wavelength of 60 μm. As shown in Ref. 43, the imprint efficiency for more-oblique beams is lower because these beams see an effectively longer length of plasma on the way to the ablation surface than the less-oblique beams; therefore, plasma smoothing is more effective for larger-angle-of-incidence beams.[43] Figure 98.32(a) shows the effect of SSD on imprint reduction. The imprinting amplitudes (of 23° and 48° beams) are reduced by a factor of ~2.5 at a spatial wavelength of 60 μm.

Conclusions

The first measurements of imprint efficiency for laser beams incident at two different angles (23° and 48°) to a target normal have been presented. The measurements were performed at a spatial wavelength of 60 μm with and without smoothing by spectral dispersion (SSD). The imprinted amplitudes were calibrated with preimposed, 60-μm-wavelength perturbations during the linear phase of RT growth. The measured imprint efficiencies at the spatial wavelength of 60 μm were 2.5±0.2 μm for the beam with a 48° angle of incidence and 3.0±0.3 μm for the beams with a 23° angle of incidence. The SSD reduced modulations by a factor of ~2.5 at the same spatial wavelength.

ACKNOWLEDGMENT

This work was supported by the U.S. Department of Energy Office of Inertial Confinement Fusion under Cooperative Agreement No. DE-FC03-92SF19460, the University of Rochester, and the New York State Energy Research and Development Authority. The support of DOE does not constitute an endorsement by DOE of the views expressed in this article.

REFERENCES

1. J. Nuckolls *et al.*, Nature **239**, 139 (1972).
2. S. E. Bodner, D. G. Colombant, J. H. Gardner, R. H. Lehmberg, S. P. Obenschain, L. Phillips, A. J. Schmitt, J. D. Sethian, R. L. McCrory, W. Seka, C. P. Verdon, J. P. Knauer, B. B. Afeyan, and H. T. Powell, Phys. Plasmas **5**, 1901 (1998).
3. J. D. Lindl, *Inertial Confinement Fusion: The Quest for Ignition and Energy Gain Using Indirect Drive* (Springer-Verlag, New York, 1998), Chap. 6, pp. 61–82.
4. M. H. Emery *et al.*, Phys. Fluids B **3**, 2640 (1991).
5. M. Desselberger *et al.*, Phys. Rev. Lett. **68**, 1539 (1992).
6. M. Desselberger *et al.*, Phys. Rev. Lett. **74**, 2961 (1995).
7. M. Dunne *et al.*, Phys. Rev. Lett. **75**, 3858 (1995).
8. R. J. Taylor *et al.*, Phys. Rev. Lett. **76**, 1643 (1996).
9. D. H. Kalantar, M. H. Key, L. B. Da Silva, S. G. Glendinning, J. P. Knauer, B. A. Remington, F. Weber, and S. V. Weber, Phys. Rev. Lett. **76**, 3574 (1996).
10. S. G. Glendinning, S. N. Dixit, B. A. Hammel, D. H. Kalantar, M. H. Key, J. D. Kilkenny, J. P. Knauer, D. M. Pennington, B. A. Remington, R. J. Wallace, and S. V. Weber, Phys. Rev. E **54**, 4473 (1996).
11. R. G. Watt, D. C. Wilson, R. E. Chrien, R. V. Hollis, P. L. Gobby, R. J. Mason, R. A. Kopp, R. A. Lerche, D. H. Kalantar, B. MacGowan, M. B. Nelson, T. Phillips, P. W. McKenty, and O. Willi, Phys. Plasmas **4**, 1379 (1997).
12. R. J. Taylor *et al.*, Phys. Rev. Lett. **79**, 1861 (1997).
13. C. J. Pawley *et al.*, Phys. Plasmas **4**, 1969 (1997).
14. S. V. Weber, S. G. Glendinning, D. H. Kalantar, M. H. Key, B. A. Remington, J. E. Rothenberg, E. Wolfrum, C. P. Verdon, and J. P. Knauer, Phys. Plasmas **4**, 1978 (1997).
15. D. H. Kalantar, M. H. Key, L. B. Da Silva, S. G. Glendinning, B. A. Remington, J. E. Rothenberg, F. Weber, S. V. Weber, E. Wolfrum, N. S. Kim, D. Neely, J. Zhang, J. S. Wark, A. Demir, J. Lin, R. Smith, G. J. Tallents, C. L. S. Lewis, A. MacPhee, J. Warwick, and J. P. Knauer, Phys. Plasmas **4**, 1985 (1997).
16. H. Azechi *et al.*, Phys. Plasmas **4**, 4079 (1997).
17. E. Wolfrum *et al.*, Phys. Plasmas **5**, 227 (1988).
18. A. L. Velikovich *et al.*, Phys. Plasmas **5**, 1491 (1998).
19. S. G. Glendinning, S. N. Dixit, B. A. Hammel, D. H. Kalantar, M. H. Key, J. D. Kilkenny, J. P. Knauer, D. M. Pennington, B. A. Remington, J. Rothenberg, R. J. Wallace, and S. V. Weber, Phys. Rev. Lett. **80**, 1904 (1998).

20. R. G. Watt, J. Duke, C. J. Fontes, P. L. Gobby, R. V. Hollis, R. A. Kopp, R. J. Mason, D. C. Wilson, C. P. Verdon, T. R. Boehly, J. P. Knauer, D. D. Meyerhofer, V. Smalyuk, R. P. J. Town, A. Iwase, and O. Willi, Phys. Rev. Lett. **81**, 4644 (1998).

21. V. A. Smalyuk, T. R. Boehly, D. K. Bradley, V. N. Goncharov, J. A. Delettrez, J. P. Knauer, D. D. Meyerhofer, D. Oron, and D. Shvarts, Phys. Rev. Lett. **81**, 5342 (1998).

22. V. A. Smalyuk, T. R. Boehly, D. K. Bradley, V. N. Goncharov, J. A. Delettrez, J. P. Knauer, D. D. Meyerhofer, D. Oron, D. Shvarts, Y. Srebro, and R. P. J. Town, Phys. Plasmas **6**, 4022 (1999).

23. D. G. Colombant *et al.*, Phys. Plasmas **7**, 2046 (2000).

24. V. N. Goncharov, S. Skupsky, T. R. Boehly, J. P. Knauer, P. McKenty, V. A. Smalyuk, R. P. J. Town, O. V. Gotchev, R. Betti, and D. D. Meyerhofer, Phys. Plasmas **7**, 2062 (2000).

25. A. J. Schmitt *et al.*, Phys. Plasmas **8**, 2287 (2001).

26. T. R. Boehly, V. N. Goncharov, O. Gotchev, J. P. Knauer, D. D. Meyerhofer, D. Oron, S. P. Regan, Y. Srebro, W. Seka, D. Shvarts, S. Skupsky, and V. A. Smalyuk, Phys. Plasmas **8**, 2331 (2001).

27. M. Nishikino *et al.*, Phys. Plasmas **9**, 1381 (2002).

28. M. Nakai *et al.*, Phys. Plasmas **9**, 1734 (2002).

29. S. P. Obenschain *et al.*, Phys. Plasmas **9**, 2234 (2002).

30. T. Endo *et al.*, Phys. Rev. Lett. **74**, 3608 (1995).

31. R. Ishizaki and K. Nishihara, Phys. Rev. Lett. **78**, 1920 (1997).

32. V. N. Goncharov, Phys. Rev. Lett. **82**, 2091 (1999).

33. Y. Lin, T. J. Kessler, and G. N. Lawrence, Opt. Lett. **20**, 764 (1995).

34. T. R. Boehly, V. A. Smalyuk, D. D. Meyerhofer, J. P. Knauer, D. K. Bradley, R. S. Craxton, M. J. Guardalben, S. Skupsky, and T. J. Kessler, J. Appl. Phys. **85**, 3444 (1999).

35. S. P. Regan, J. A. Marozas, J. H. Kelly, T. R. Boehly, W. R. Donaldson, P. A. Jaanimagi, R. L. Keck, T. J. Kessler, D. D. Meyerhofer, W. Seka, S. Skupsky, and V. A. Smalyuk, J. Opt. Soc. Am. B **17**, 1483 (2000).

36. T. R. Boehly, D. L. Brown, R. S. Craxton, R. L. Keck, J. P. Knauer, J. H. Kelly, T. J. Kessler, S. A. Kumpan, S. J. Loucks, S. A. Letzring, F. J. Marshall, R. L. McCrory, S. F. B. Morse, W. Seka, J. M. Soures, and C. P. Verdon, Opt. Commun. **133**, 495 (1997).

37. R. H. Lehmberg and S. P. Obenschain, Opt. Commun. **46**, 27 (1983).

38. H. Nakano *et al.*, J. Appl. Phys. **73**, 2122 (1993).

39. Y. Aglitskiy *et al.*, Phys. Rev. Lett. **87**, 265001 (2001).

40. Y. Aglitskiy *et al.*, Phys. Rev. Lett. **87**, 265002 (2001).

41. Y. Aglitskiy *et al.*, Phys. Plasmas **9**, 2264 (2002).

42. R. L. McCrory and C. P. Verdon, in *Computer Applications in Plasma Science and Engineering*, edited by A. T. Drobot (Springer-Verlag, New York, 1991), Chap. 11, pp. 291–325.

43. V. A. Smalyuk, J. A. Delettrez, S. B. Dumanis, R. Epstein, V. Yu. Glebov, D. D. Meyerhofer, P. B. Radha, T. C. Sangster, C. Stoeckl, N. C. Toscano, J. A. Frenje, C. K. Li, R. D. Petrasso, F. H. Séguin, and J. H. Koch, "Hot-Core Characterization of the Cryogenic D_2 Target at Peak Neutron Production in Direct-Drive Spherical Implosion," to be submitted to Physical Review Letters.

44. V. A. Smalyuk, T. R. Boehly, D. K. Bradley, J. P. Knauer, and D. D. Meyerhofer, Rev. Sci. Instrum. **70**, 647 (1999).

45. J. Delettrez, R. Epstein, M. C. Richardson, P. A. Jaanimagi, and B. L. Henke, Phys. Rev. A, Gen. Phys. **36**, 3926 (1987).

46. M. J. Dunning and S. W. Haan, Phys. Plasmas **2**, 1669 (1995).